Electronic Supplementary Information:

Ultra-fast electron capture by an electrosterically-stabilized metal nanoparticle

Khashayar Ghandi[1], Alexander D. Findlater[2], Zahid Mahimwalla[1], Connor S. MacNeil[1], Ernest Awoonor-Williams[1], Federico Zahariev[2], Mark S. Gordon[2*]*

[1]Department of Chemistry & Biochemistry, Mount Allison University, Sackville, NB, Canada, E4L 1G8

[2]Department of Chemistry and Ames Laboratory, Iowa State University, Ames, Iowa, USA, 50011-3020

*Corresponding Author: Khashayar Ghandi, Department of Chemistry & Biochemistry, Mount Allison University, Sackville, NB, Canada, E4L 1G8, Phone: 1 (506) 364-2370, Email: kghandi@mta.ca

I. Gold Nanoparticle [AuNP] Synthesis and Concentration Determination

Benzyldimethyltetradecylammonium chloride, bac-14 [TCI-America] is a room temperature ionic liquid [RTIL] and cationic surfactant, used as a protecting group and stabilizing agent. Sodium borohydride, $NaBH_4$ is used as a reducing agent promoting the reduction of the gold [$Au^{III} \rightarrow Au^0$] in water, as evidenced by the disappearance of the absorbance peak at 340-400 nm. The synthesis is carried out as follows. In a 250 mL round bottom flask aqueous $HAuCl_4$ [25 mL, 2.5 mmol] was stirred at 40 °C under a reduced atmosphere of Nitrogen [Praxair 99.997%] for 15 minutes. Bac-14 [4 g, 10 mmol] was then added to 60 mL water and combined with the aqueous $HAuCl_4$ solution to produce a yellow-solution. $NaBH_4$ [800 mg, 21 mmol] was added to 15 mL of distilled deionized water and the resulting solution added dropwise to the reaction mixture over several minutes. Reduction was instantaneous and the mixture was allowed to stir under mild heat for 2-3 hours. Figure S1 is a TEM image of as prepared gold nanoparticles, electrosterically stabilized with bac-14.

Our synthesis maximizes atom economy by eliminating the use of a phase transfer catalyst in an aqueous organic bilayer, which involves complicated intermediates.[1,2] The surfactant [bac-14] contains a benzyl moiety and a chloride counter ion [Fig. 1] that stabilizes agglomerating Au atoms through electrostatic and steric interactions (electrosteric).[3] The inclusion of the benzyl moiety contributes to the stability of the NP framework via π-π/ion stacking and provides an unsaturated site for the addition of free radicals. The water-based synthesis is considerate of the negative environmental impact of organic solvents as well as possible medical applications compared to more conventional AuNPs synthesis procedures [i.e., toluene, hexanes, and benzene solvents].

The morphologies and composition of the gold nanoparticles [AuNPs] were characterized using a scanning electron microscope [JEOL JSM-5600 SEM operating at 10kV] and a scanning/transmission electron microscope [JEOL 2011 STEM, operating at 200kV, combined with energy disperse X-ray spectroscopy [EDX] detection. The surface plasmon resonance of solution-based AuNPs was measured using a Cary-100 UV-Vis spectrometer with maximum absorbance observed near 520 nm. All samples submitted for UV-Vis spectroscopy were diluted by a factor of 1/100. Attenuated total reflectance [ATR] spectroscopy was performed on the samples using a Thermo Scientific Nicolet iS5 spectrometer equipped with an iD5 ATR accessory.

FT-IR and UV-Vis measurements were taken at different stages during the synthetic procedure. UV-Vis confirms the reduction of Au^{III} to Au^{0} in the disappearance of the peak near 320-400 nm in the intermediate spectrum, which is apparent in the unreduced aqueous $HAuCl_4$ starting material. The appearance of the SPR peak at or near 520 nm [fig. S2] confirms successful formation of gold nanoparticles and is observed in the product spectra.

A previously published method by Liu *et. al*. was used to calculate the concentration of gold nanoparticles in solution.[4,5] Using TEM [Fig. S1], the average core diameter of the AuNPs was determined using ImagePro Plus software; $D = 9 \pm 3$ nm, the average number of gold atoms in a nano-particle was calculated according to equation S1.

$$N = [\pi/6][\rho/M]\cdot D^3 \qquad [S1]$$

Where ρ is the density of fcc gold, 19.3 g cm^{-3} and M is the molar mass of gold, 197 g mol^{-1}. An average core diameter of 9 nm would then result in an average number of gold atoms in a nanoparticle of 2×10^4. The molar concentration of gold nanoparticle suspended in solution is then 2×10^{-6} mol L^{-1} according to equation 2.

$$c = N_{total}/NVN_A \qquad [S2]$$

where N_{total} is the total number of gold atoms in the solution. The molar absorptivity (extinction coefficient) was calculated according to the Beer-Lambert law, eq. 3.

$$A_{spr} = \varepsilon bc \qquad [S3]$$

We report here $\varepsilon = 1.82 \times 10^8\ M^{-1}\ cm^{-1}$ which compared well to the literature. Despite differences in the synthetic method of AuNPs used by Liu *et. al.*, as compared the Au/bac-14 nanoparticle, fit well within these relationships (figures S4 and S5).

II. Kinetics – Determination of rate constants for electron capture

For the concentrations of AuNPs prepared from the novel one-pot synthesis outlined above, we assume a pseudo-first/first order reaction rate since the concentration of electrons from single muon irradiation of the sample at any time should be much smaller than the concentration of nanoparticles.[6] Muon thermalization occurs on the sub nanosecond timescale. The rate of electron capture can be described by equation 4.

$$v = k_e[\text{AuNP}] \qquad \textbf{[S4]}$$

Where, k_e is the effective rate constant $[M^{-1}\ s^{-1}]$ and [AuNP] is the concentration of gold nanoparticles and v is the minimum rate of ~ 1 ns^{-1}.

Based on the concentration determination above, we calculate the effective rate constant $[M^{-1}\ s^{-1}]$ is $5 \times 10^{14}\ M^{-1}s^{-1}$ for a gold nanoparticle concentration of 2×10^{-6} mol L^{-1}.

III. Muon Spin Rotation

In the transverse-field [TF] μSR experiment performed, the degassed gold nanoparticle solution was placed in a target cell comprised of thick, non-magnetic, stainless steel walls as well as inside a vacuum insulation jacket. Muons are fired at this vessel and enter the cell via a 1/1000 inch thick and 1.25 cm radius entrance window. In TF- μSR experiments, a magnetic field is applied transversely to the spin of the muon, causing the spin of 100% spin polarized particles to precess about this field. The muons' decay positrons can map out this precession. Before entering the sample cell, the muon activates a muon counter, starting a fast electronic clock. Once in the sample, its spin will precess about the given magnetic field at a frequency specific to the muon's magnetic environment and gyromagnetic ratio until the muon decays after ~2.2 μs, with a positron being emitted preferentially along the direction of the spin. Scintillators located outside the sample cell detect these events, corresponding individually to the detection of one muon entering the sample and the detection of its corresponding positron. The positrons upon hitting the scintillators result in the emission of photons detected by photomultiplier tubes [PMT]. Each detected event is placed in a histogram. This allows the characterization of the muon spin precession in its specific magnetic environment. Temperature in the experiment was controlled by fluid filled copper tubes and measured using thermocouples [TCs]. TRIUMF's 'Helios' μSR spectrometer was used for this study, with transverse fields applied of at most 12 kG in magnitude. Four counters [the aforementioned scintillators located outside the sample cell] were set up in quadrature in the plane of precession [Up Right, Down Right, Up Left, Down Left] and used to detect the muon's decay positrons.

IV. Calculations of the Diffusion Limit for Nanoparticle Reactions

A combined model for kinetic diffusion was used to estimate the rate of electron capture based on the modified Stokes-Einstein form for spherical [uncharged] particles through a liquid of low Reynolds number, taking into account the diffusion coefficient D for the electron. Using data reported by Schmidt and co-workers, kinetic diffusion for hydrated electrons at ambient temperatures and atmospheric pressure in H_2O,[7] $D = [4.90 \pm 0.02] \times 10^{-5}\,cm^2\,s^{-1}$. An independent report on TiO_2 nanoparticles capped with *p*-toluenesulfonic acid with the size ~6 nm showed that $D = 10^{-10}\,m^2\,s^{-1}$.[8]

The rate constant of a diffusion-controlled reaction is given as $k_d = 4\pi R^* D N_A$, where two reactant molecules react if they come a distance R^* from each other. In this case, diffusion of small molecules to the surface of a nanoparticle is faster if the particle is larger. Given the size of the gold nanoparticles [9 nm], the center-to-center distance R^* is close to the radius of the nanoparticle r (this is minimum distance for reaction, however larger distance is certainly expected as 1) the pre-solvated ("dry electron") electron is not localized, 2) there is a large probability of quantum tunneling over longer distance for more wave like electrons). Using $k_d = 4\pi R^* D N_A$ where N_A is Avogadro's number.

The rate of nanoparticle-electron combination should be defined by the diffusion of the electron, given that the kinetic diffusion is remarkably fast in water. The model predicts, $k_d \sim 5 \times 10^{14}\,M^{-1}s^{-1}$, which is agreement with experiment. This relationship is plotted in figure S8. Based on this result we expect a larger rate constant for larger gold nanoparticles.

Supporting Figures S1-S8

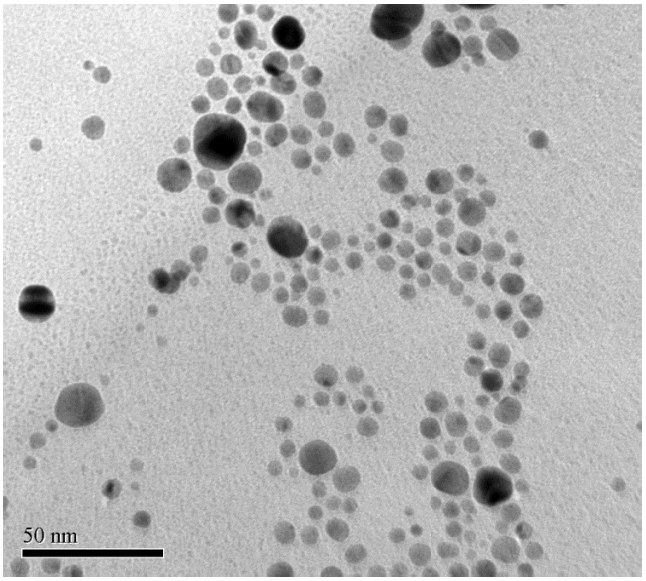

Figure S1. TEM image of as prepared gold nanoparticle. Size distribution is normally distributed. Average diameter is 24 nm

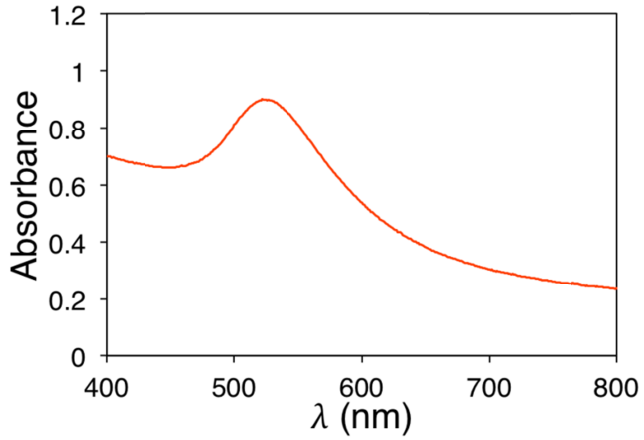

Figure S2. UV-visible spectrum depicting surface plasmon band of Au/bac-14 AuNPs synthesized by a single-phase process described above. Surface plasmon band is observed with max wavelength at 520 nm.

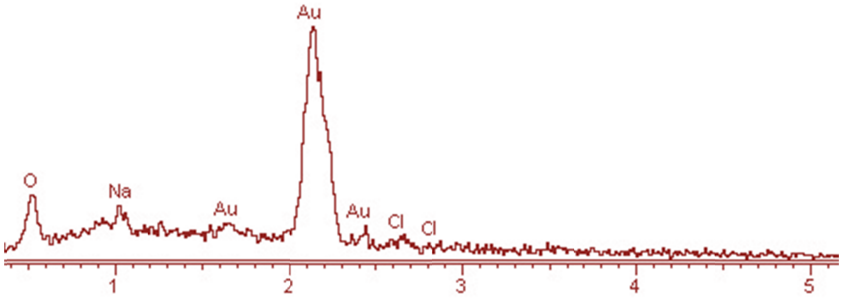

Figure S3. EDX analysis of Au/bac-14 as prepared in water. The carbon peak from the substrate is omitted to observe nearby peaks.

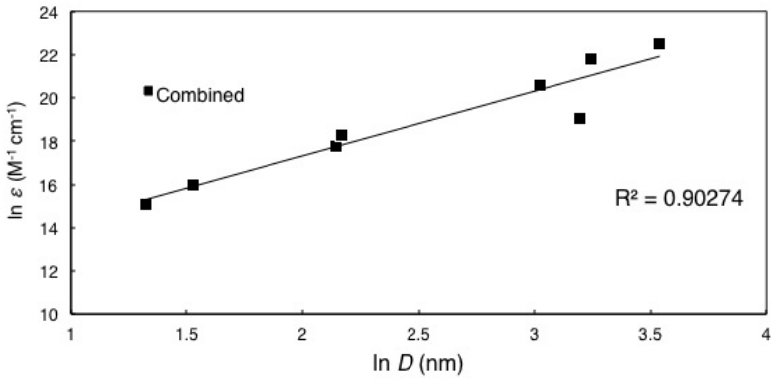

Figure S4. A plot of ε [M^{-1} cm^{-1}] versus core diameter of gold nanoparticles from [5] capped with citrate, decanethiol, or oleylamine.

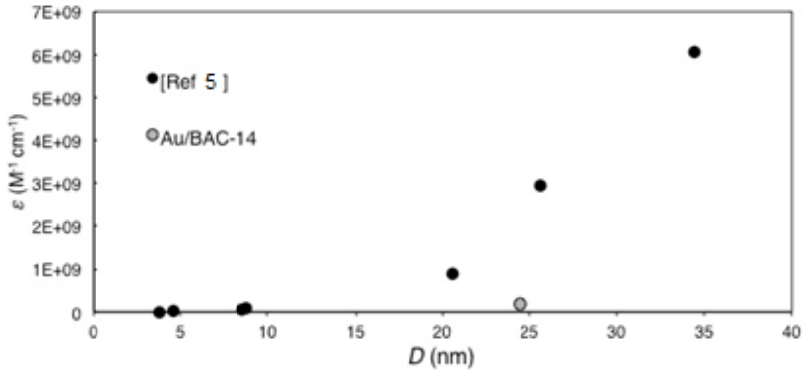

Figure S5. A double logarithmic plot of ε [M^{-1} cm^{-1}] versus core diameter of gold nanoparticles from [5] capped with citrate, decanethiol, or oleylamine. Linear fit of all AuNPs is > 0.9.

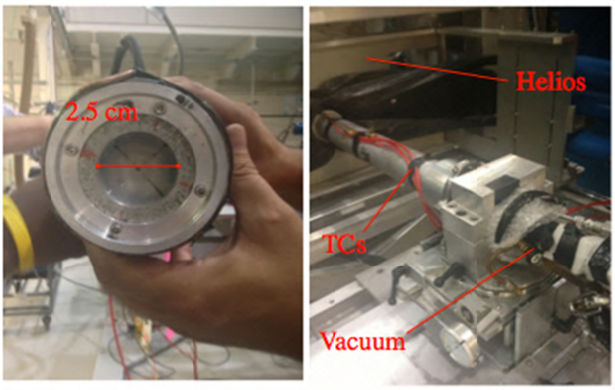

Figure S6. Photographs of the TRIUMF Helios μSR spectrometer. Left, the vacuum jacket assembly in which the target cell is placed. Right, the assembled, target assembly placed into the Helios spectrometer.

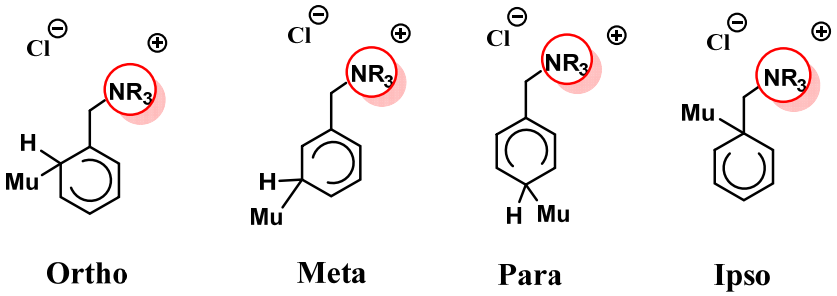

Figure S7. Sites of Muonium addition in bac-14.

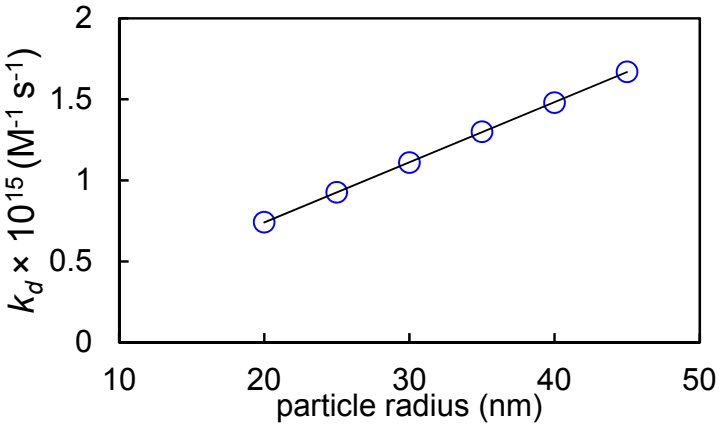

Figure S8. Calculated rate constant [10^{15} M^{-1} s^{-1}] of electron-nanoparticle reaction based on a modified Stokes-Einstein kinetic form. Rate constants scale linearly with particle size [nm].

V. Supplementary text

$$\mu^+ + e^- \rightarrow \text{Mu} \qquad \text{[S5]}$$

$$\mu^+ + \text{H}_2\text{O} \rightarrow \rightarrow \text{MuH}_2\text{O}^+ \qquad \text{[S6]}$$

$$e^-_{aq} + \text{MuH}_2\text{O}^+ \rightarrow \text{Mu} + \text{H}_2\text{O} \qquad \text{[S7]}$$

$$\text{H}_2\text{O} + \text{MuH}_2\text{O}^+ \rightarrow \text{MuOH} + \text{H}_3\text{O}^+ \qquad \text{[S8]}$$

$$\text{Mu} + e^-_{aq} + \text{H}_2\text{O} \rightarrow \text{MuH} + \text{OH}^- \qquad \text{[S9]}$$

$$e^- + \text{AuNP}_{aq} \rightarrow \text{AuNP}^-_{aq} \qquad \text{[S10]}$$

$$\text{Mu} + \text{C}_6\text{H}_6 \rightarrow \text{C}_6\text{H}_6\text{Mu}^\bullet \qquad \text{[S11]}$$

The dynamics of electron capture is assessed using muon spin rotation, with observed electron capture inferred from the interaction of spin-polarized muons with the environment. Free radicals are characterized through a hyperfine interaction, or coupling between spin-active nuclei and the unpaired electron. The isotropic hyperfine coupling constant [hfcc], is a measure of the unpaired electron density at the nucleus $|\psi[0]|^2$. For muoniated organic radicals, muon hfccs are in the range from a few MHz to several hundred MHz.

The muon hfcc is obtained by frequencies, ν_{12} and ν_{43}. In high-fields these frequencies are given by

$$\nu_{12} = \nu_{\text{mid}} - 1/2A_\mu \qquad \text{[S12]}$$

$$\nu_{43} = \nu_{\text{mid}} + 1/2A_\mu \qquad \text{[S13]}$$

$$A = \left|\nu_{12} - \nu_{43}\right| \qquad \text{[S14]}$$

where ν_{mid} is equal to the spin precession of muons in diamagnetic environments [ν_D = 0.01355 MHz G^{-1}] and is typically the largest peak in a TF-spectrum. It is sometimes the case, not excluding this work, that the higher precession frequency ν_{43} is too small. The hyperfine coupling is then calculated using equation S14. There are four symmetry-distinct/unique sites of addition in the aromatic ring of bac-14, whereas for benzene, D_6h symmetry provides only one. Notwithstanding the possible product of the addition to chloride anion [hfcc > 1000 MHz], *para-, ortho-, meta-,* and *ipso*-addition sites were considered relative to the alkyl substituent [fig. S7].

The radical formed here is centered on the benzyl ring of bac-14 by necessity given the sites of unsaturation. The model radical used to compare aromatic systems is the cyclohexadienyl radical, which forms from the addition of Muonium [Mu, S11] to the sites of unsaturation in benzene. The addition reaction to a C-C double bond is typically two orders of magnitude faster than abstraction, and dominates here. The cyclohexadienyl radical is characterized by a hyperfine coupling of *c.a.* 515 MHz between the methylene muon [proton] and the unpaired electron in the ring.

Recognizing the structural similarities of the cyclohexadienyl radical [C_6H_6Mu] and the bac-14 radical [See Fig. 3, bottom, for a model of the bac-14 radical in which the alkyl chains are modeled with methyl groups], their respective hfccs were compared. Benzene is a D_{6h} symmetric molecule, allowing Mu to be non-discriminately absorbed onto any of the carbons. The resulting methylene proton [muon] spin couples with the unpaired electron spin in the ring. This hyperfine interaction has been well-studied and serves as a model for radical addition to aromatic rings. The muon hfcc [A_μ] in C_6H_6Mu is ca. 515 MHz. A decreased magnitude of A_μ was observed in the bac-14 radical, owing to the transfer of unpaired spin-density to the β-nitrogen.

The identity of these radicals is facilitated using computational chemistry. Specifically through the calculation of isotropic Fermi contact coupling of different nuclei. Here, Muonium addition across each of the double bonds in the aromatic ring is calculated, resulting in different hfcc values depending upon the site of addition. For the *para*-addition, a calculated hfcc of 138.53247 MHz is obtained. This value is multiplied by a correctional factor of 851.6/267.5 [3.1833], which is the ratio of the muon and proton gyromagnetic ratios, γ_n. These calculated values agree reasonably well with experiment.

The formation of paramagnetic species, including Mu and free radicals, reduce the diamagnetic fraction, as characterized by the Larmor frequency of the muon, 0.01355 MHz G^{-1}. At an applied field of 10 kG, we observe a characteristic frequency *ca.* 135 MHz. At the reference concentration [0.1 M] the presence of free radicals was observed due to the addition of $^{0.11}$H to bac-14 in the absence of AuNP. $^{0.11}$H addition was determined by analysis of the muon hyperfine coupling constants [hfcc] [which are directly related to the peaks in the Fig. 3 spectrum with hfcc magnitudes indicating the extent of delocalization of the unpaired electron over the molecule.

Table S1: Calculated Isotropic Fermi Contact Coupling between proton/muon and unpaired electron.

		A_{iso} [theory] / MHz	A_{iso} [Mu] / MHz
	nuclei	B3LYP/6 –31G*	B3LYP/6 –31G*
para	^{1}H [top]	138.532	441
	^{1}H [bottom]	139.127	442
ortho	^{1}H	135.674	430
meta	^{1}H [top]	142.845	455
	^{1}H [bottom]	144.784	461
ipso	^{1}H	128.776	409

References

1. M. Brust, M. Walker, D. Bethell, D. J. Schiffrin, and R. Whyman, *J. Chem. Soc. Chem. Commun.*, 1994, 801.
2. P. J. G. Goulet and R. B. Lennox, *J. Am. Chem. Soc.*, 2010, **132**, 9582–4.
3. M. W. Heaven, A. Dass, P. S. White, K. M. Holt, and R. W. Murray, *J. Am. Chem. Soc.*, 2008, **130**, 3754–5.
4. M. Farren-Dai, E. Awoonor-Williams, C. S. MacNeil, Z. Mahimwalla, and K. Ghandi, *Chem. Phys. Lett.*, 2014, **610-611**, 331–334.
5. X. Liu, M. Atwater, J. Wang, and Q. Huo, *Colloids Surf. B. Biointerfaces*, 2007, **58**, 3–7.
6. P. Percival, E. Roduner, and H. Fischer, *Chem. Phys.*, 1978, **32**, 353–367.
7. K. H. Schmidt, P. Han, and D. M. Bartels, *J. Phys. Chem.*, 1992, **96**, 199–206.
8. L. Van Lokeren, G. Maheut, F. Ribot, V. Escax, I. Verbruggen, C. Sanchez, J. C. Martins, M. Biesemans, and R. Willem, *Chemistry*, 2007, **13**, 6957–66.